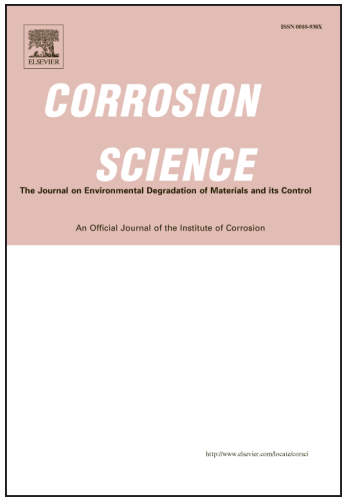

Grain Boundary Oxidation in Iron-Based Alloys, investigated by ^{18}O enriched Water Vapour - The Effect of Mixed Oxides in binary and ternary Fe-{Al, Cr, Mn, Si} Systems

Michael Auinger, Vera G. Praig, Bernhard Linder, Herbert Danninger

PII: S0010-938X(15)00169-9
DOI: http://dx.doi.org/10.1016/j.corsci.2015.04.009
Reference: CS 6273

To appear in: *Corrosion Science*

Received Date: 30 October 2014
Accepted Date: 4 April 2015

Please cite this article as: M. Auinger, V.G. Praig, B. Linder, H. Danninger, Grain Boundary Oxidation in Iron-Based Alloys, investigated by ^{18}O enriched Water Vapour - The Effect of Mixed Oxides in binary and ternary Fe-{Al, Cr, Mn, Si} Systems, *Corrosion Science* (2015), doi: http://dx.doi.org/10.1016/j.corsci.2015.04.009

Grain Boundary Oxidation in Iron-Based Alloys, investigated by ^{18}O enriched Water Vapour - The Effect of Mixed Oxides in binary and ternary Fe-{Al, Cr, Mn, Si} Systems

Michael Auinger [a,c,e,*], Vera G. Praig [b,c,**], Bernhard Linder[d], Herbert Danninger[b,c]

[a] *Max-Planck-Institut für Eisenforschung GmbH, Max-Planck-Strasse 1, D-40237 Düsseldorf, GERMANY*
[b] *Institute for Chemical Technologies and Analytics, Vienna University of Technology, Getreidemarkt 9, A-1060 Vienna, AUSTRIA*
[c] *Christian Doppler Laboratory for Diffusion and Segregation Processes during Production of High Strength Steel Sheets*
[d] *voestalpine Stahl GmbH, voestalpine-Straße 3, A-4020 Linz, AUSTRIA*
[e] *WMG, International Manufacturing Centre, University of Warwick, Coventry CV4 7AL, UNITED KINGDOM*

Abstract

Selective oxidation experiments at 700 °C in binary and ternary iron-based model alloys containing Al, Cr, Mn, and Si were carried out. The internal oxidation behaviour along grain boundaries and inside ferrite grains was analyzed by LOM, SEM and ToF-SIMS. Oxygen isotope exchange revealed the location of fast diffusion pathways in the alloy. Numerical calculations of oxide distributions were compared to experimental findings, revealing that oxygen transport within ferrite grains is significantly lower than reported from literature. Discrepancies between simulations and experiments were

*Dr. Michael AUINGER (michael.auinger.at@ieee.org)
**Dr. Vera G. PRAIG (vera.praig@tuwien.ac.at)

discussed. The presented hypothesis of oxygen trapping represents an important viewpoint to explain internal oxidation in metallic alloys.

Keywords: A. Steel, A. Alloy, B. Modelling Studies, C. High temperature corrosion, C. Selective oxidation, C. Internal oxidation

1. Introduction

Steels and other corrosion resistant alloys are an important backbone for applications in the automotive and construction industry as well as for novel energy conversion technologies [1, 2]. However, a safe application of those materials in highly corrosive atmospheres such as for gas turbine blades [3], propulsion engines, boiler steels [4, 5] or waste incineration plants [6] necessitates the formation of a protective layer that hinders further corrosive attack at elevated temperatures [1, 2, 7, 8]. Other than that, oxidation plays an essential role during the manufacturing of steels for automotive applications. Here, high-strength materials that often contain manganese (such as TRIP/TWIP-steels [9]) are frequently used because of their unique mechanical properties. This allows a significant reduction of sheet thickness and as a consequence the vehicle becomes lighter, which helps to reduce carbon dioxide emissions and meets today's emission criteria as well as the ideas of modern energy politics.

During manufacturing of a sheet material, the alloy undergoes a series of high temperature treatments in oxygen-rich atmospheres, which are often combined with plastic deformation. Hot-rolling of slabs has proven to be quite effective for quick size reduction and good mechanical properties of the final sheet material. However, oxide formation underneath the materials surface

(so-called "internal oxidation" [10]) becomes problematic as the hot-rolled sheet is only rapidly cooled down to temperatures between 600 and 800 °C before coiling. The hot coil is then left to cool in the ambient atmosphere, which occurs during a time-frame of several hours. Here, the initially formed wüstite layer (iron oxide at the surface) acts as an oxygen reservoir for internal oxidation of the alloy additions - both inside the grains (termed "bulk oxidation") and along grain boundaries [11, 12]. Whereas bulk oxidation represents a rather complex discipline that combines reaction kinetics, element transport, defects chemistries [13], nucleation, interface properties and many more, grain boundary oxidation is strongly connected to the atomic structure of grain boundaries [14, 15]. Especially oxides along grain boundaries weaken the cohesion between individual grains, which may even fall off after subsequent forming processes (e.g. for view parts in automotive industry). Therefore, an in-depth understanding of transport properties and oxidation at high temperatures becomes vitally important to invent novel protection strategies against high temperature corrosion. Beside the many works on high temperature oxidation of steels and nickel-based alloys, only little is reported on the corrosion properties of well-defined model systems [16, 17, 18]. Hence, this work aims at providing a fundamental understanding of grain boundary oxidation in iron-based alloys, including the four most important metallic alloy additions in steel manufacturing - aluminium, chromium, manganese and silicon [9, 19]. Mixtures of hydrogen and water vapour were used in this study to mimic the selective oxidation condition underneath the outer scale layer [20, 21], generating a scenario with maximal internal oxidation. Furthermore, the exchange of the oxygen isotopes (^{16}O to ^{18}O) during ex-

posure helps to determine the pathways of fast oxygen diffusion into the material and to elucidate the origin of oxygen transport. Although the oxygen transport [22, 23] and the decomposition kinetics of the wüstite phase [24] often determine the oxygen activity at the metal-scale interface - which may differ from the experimental conditions in this study - this approach provides a fundamental understanding of alloy composition on oxide formation [18]. Numerical simulations were carried out to predict the internal oxidation behaviour and local (oxide) phase distribution [21, 25]. The results from calculations are compared to the experimental findings and critically discussed.

2. Experimental

Hot rolled iron-based alloy samples (in house production; see table B.1) were cut into square shaped pieces of 15 mm × 15 mm × 1 mm in size. All surfaces were mechanically ground by using grinding papers from 400 down to 2500 grit size, to ensure an optimal compromise between sample roughness and the efficiency of sample heating in an infra-red furnace [26]. Prior to exposure, all samples were ultrasonically cleaned in ethanol and dried in a cold stream of dry air.

(TABLE 1)

Selective oxidation experiments were carried out at 700 °C for a total time of 60 min in a horizontal infra-red furnace, equipped with a vacuum pump and connected to a 8 L gas mixing chamber. Details of the experimental set-up have been published previously [27] and can also be found in

figure $B.1$. The sample temperature was measured by a Ni/CrNi thermocouple, which was pressed with a small quartz piston onto the sample surface. Gas exchange after 30 min has been achieved by closing the first gas line, evacuating the reaction chamber with a turbo-molecular pump and switching to the gas mixture from the gas mixing chamber. Two mixtures of Ar/H_2 (97.5/2.5, v/v) with a humidity of +6 °C dew point (0.94vol-% H_2O) were used, which corresponds to an oxygen activity in the atmosphere closely below the onset of wüstite formation under these conditions (+13 °C dew point) [34]. During the first 30 min at elevated temperatures, the argon/hydrogen mixture was saturated with water vapor at +6 °C by bubbling 15 L h^{-1} (± 0.5% [27]) dry gas through deionised water. The second gas mixture, containing ^{18}O-enriched water vapour (high purity water from Sigma Aldrich, 99% $H_2^{18}O$), was prepared in a separate gas mixing chamber which had firstly been evacuated to 10^{-6} mbar. Degassed $H_2^{18}O$ was evaporated into the evacuated chamber until a pressure of 41.5 mbar was reached. After this, 112.5 mbar hydrogen was added and the chamber was filled with argon to a total pressure of 4.5 bar, yielding the same gas composition as before (97.5% Ar, 2.5% H_2, ≈0.93vol-% $H_2^{18}O$). To avoid condensation in the filled gas mixing chamber, the vessel was thermally insulated, wrapped in aluminium foil and heated up to 40 °C. The gas flow conditions from the gas mixing chamber were in the range between 15 and 8 L h^1 , depending on the actual pressure in the chamber which varied from 4.5 bar in the beginning to ≈2.5 bar at the end of the exposure. However, the pressure drop between reaction chamber and the ambient atmosphere was constant during both oxidation steps and mostly defined by the height of two filled water columns in the gas exhaust line,

that were installed to avoid oxygen back-diffusion. All process parameters during the experiment were recorded fully automatically and stored in a single protocol file by using an in-house written software routine [27]. Great care has been taken to reduce the oxygen impurity content in the reaction chamber below 10 ppm O_2. After thermal treatment, the samples were allowed to cool in the flowing gas stream, covered with an electrodeposited nickel layer (tampon galvanisation, 20-50 mA cm^{-2}, Ni-Anode, commercial $NiSO_4$ electrolyte [28]) and mounted in epoxy (PolyFast, Struers). Cross sections of the samples were prepared with a 10° tilt angle relative to the specimen surface to enlarge the oxidised zone depth by a factor of 5.67, polished with 1 μm diamond paste and analysed by means of optical microscopy (Axiovert 405M, Zeiss, Germany), scanning electron microscopy (FEI Quanta 200 k, FEI COMPANY, The Netherlands) and ToF-SIMS (TOF-SIMS 5, ION-TOF GmbH, Germany). The operation mode of the ToF-SIMS has been set to dual beam sputtering analysis by 25 keV Bi^+ (80 μm × 80 μm) and 2 keV Cs^+ (500 μm × 500 μm) presputtering, called "burst alignment" mode to enhance the sensitivity of the two different oxygen isotopes ^{16}O and ^{18}O.

3. Mathematical Modelling

Numerical simulations of the phase distributions were calculated by a subsequent two-step based algorithm "ASTRID" [29], consisting of element migration and thermodynamic reactions [21, 25, 26, 27, 30]. Transport of the atomic species (oxygen, iron and the alloying elements) has been derived from the set of partial differential equations. Diffusion coefficients were chosen from carefully selected literature sources and are listed in table B.2. Phase

diagrams of the alloy systems (see figures B.7 and B.8 in the appendix) indicate that only the diffusion properties in the ferrite phase need to be considered. This follows from the consequence that the crystal structure of the iron matrix does not undergo a phase change (α-γ transition) during heating or at the applied treatment temperature. The alloy content in the samples of this study is either too low to stabilise the austenite phase or does not stabilise the austenite phase at all. Hence, depletion of dissolved alloy element additions (Al, Cr, Mn, Si) due to oxide formation does not lead to a phase change in the experiments.

(TABLE 2)

The oxygen concentration at the surface (upper boundary) is set to a constant value, according to the maximum solubility of oxygen under given temperature and oxygen activity in the reaction gas (0.65 ppm [O], see [32], or table B.2). This corresponds to the constant source model firstly proposed by Wagner [33], which reflects the actual conditions at the sample surface in a sufficiently accurate manner. Hence, this assumption is most commonly used in theoretical simulation studies of internal oxidation [21, 25, 30, 34, 35]. The calculation of the diffusion has been carried out for small time intervals ($\leq$ 1 min). The results after each calculation step have been used to derive the local concentrations of each phase with thermodynamic subroutine ChemApp (GTT-Technologies, Germany) [36]. The amount of each phase from the equilibrium calculation was set as the starting value for the diffusion calculation in the next time interval. After the last simulation step, the results were displayed as a two-dimensional concentration map, similar to a

cross section polish of the specimen, indicating the amount and spatial distribution of each stable phase separately. For reasons of graphical simplicity, the sample microstructure was composed by hexagonal grains, separated by a 50 nm thick grain boundary domain. Theoretical results will be presented as a density distribution with values between 1 (maximum concentration) and 0. This mode of presentation has been chosen because the concentration of the alloying elements, and hence the amount of formed precipitate phases, is very low compared to the iron in the matrix.

4. Results and Discussion

Very stable process conditions during the exposure could be achieved and typical values are summarised in figure B.1. Slight overheating in the initial stages of heating can be attributed to the extremely fast heating rate of 7 K s^{-1} (see the small temperature peak in Figure B.1 at 2 min). The temperature however, quickly stabilises at 700 °C and remains constant during the remaining exposure time, except during the gas exchange where the set-temperature has been lowered by 5 K for better visualisation. Although a time frame of 7 min in the temperature program has been set for evacuation and gas exchange in the reaction chamber, this process was often finished within 4-5 min. Slight decreases of the gas flow of the ^{18}O-enriched atmosphere can be attributed to the drop of pressure in the gas mixing chamber with time. Simultaneously, the content of oxygen impurities in the reaction gas increases with time but always remains below a limit of 10 ppm O_2.
After heat treatment, the samples show a grey-shiny or even metallic surface, indicating the absence of outer scale formation, which underlines the

successful experimental conditions for avoiding the formation of an outer (iron) oxide scale [18, 37]. Results of the oxidation depths in all samples will be summarised in table $B.3$.

(TABLE 3)

4.1. Binary Alloys

Little to no signs of pure internal oxidation could be observed in the SEM pictures of figure $B.2$, as the oxide precipitates, formed inside the ferrite grains, are less than 100 nm in size. Similar to previous studies [18], a thin layer of (Fe,Mn)O could be observed near the surface of Fe-2Mn. The oxidation depth appears to be quite uniform in Fe-{1,3}Al and Fe-2Mn, whereas fine patterns of 50 nm to 200 nm thick grain boundary oxides could only be seen in Fe-0.8Cr and Fe-1Si. The structure of the grain boundary oxides in Fe-1Si appears to be homogeneously distributed and uniform in thickness, whereas in Fe-0.8Cr small oxide particles align at the grain-grain interface. Some works theorize about the existence of a continuous network of alloy precipitates ("seaweed-like structure" [38]), that forms between the metal grains as a consequence of local changes of the grain boundary orientation.

(FIGURE 2)

The differences in the bulk oxidation depth between experiments and theoretical predictions are likely to be caused by the interaction of the elements with individual oxygen traps in the metal lattice (e.g. single defects). Trapping leads to a slower diffusion rate in reality [37], compared to the ideal crystal from theoretical predictions [39]. Segregation during sample preparation

or kinetic effects of oxide phase formation may also cause minor deviations. However, grain boundary segregation of elements is quite small at elevated temperature [40, 41] and diffusion lengths into the grain are extremely short [14, 15] which would mainly affect the near-surface oxide distribution during the initial stages of oxidation.

Surface and interface energies can have a detrimental influence on oxide nucleation, which may hamper the formation of individual phases. It is well known that the formation of hexagonal chromia nuclei in a cubic ferrite environment is kinetically hindered [1, 2]. Consequently, local supersaturation of oxygen in the ferrite matrix and - in extreme cases - the direct conversion of dissolved chromium into the spinel phase has been observed [42]. In the case of aluminium, it is known that cubic θ-Al_2O_3 forms initially and then slowly transforms into the more stable α-Al_2O_3 phase (trigonal) [43]. Due to this behaviour, the energy barrier for oxide formation and hence local oxygen supersaturation in the metal are minimised.

Polycrystalline oxides such as MnO and spinels [44] possess a quite high oxygen diffusion coefficient, compared to pure Al_2O_3, Cr_2O_3 and SiO_2 at given oxygen activities in this study [7, 22, 45]. Hence their presence should not block the internal oxidation process completely and would allow the observation of pronounced grain boundary oxide formation in the material. Despite the fact that manganese is an element that easily switches between its valency states, grain boundary oxidation in pure iron-manganese samples was not observed. This indicates that the formation of defect-rich oxides with relatively high ion mobilities alone does not lead to enhanced grain boundary oxidation.

4.2. Ternary Alloys

Light optical micrographs of the metallographic sections revealed clear signs of internal oxidation, as shown in figure B.3. Remarkably, the ternary alloy compositions containing 2 wt-%Mn show a well-pronounced oxide formation along grain boundaries (figure B.3, left column) forming a wavy pattern of the oxide front. The total oxidation depth in these alloys is governed by the large network of thin oxides along the intergranular region and reaches values between 7 μm (Fe-2Mn-0.8Cr) and 10 μm (Fe-2Mn-1Si). A homogeneous zone of bulk oxides can be seen in the cases of manganese-free alloys containing silicon, aluminium or chromium (figure B.3, right column). Within this group of materials, indications of an enhanced oxide formation along grain boundaries could only be seen in the case of Fe-3Al-0.8Cr (4.5 μm). The presence of grain boundary oxides, however, has only minor influence on the total oxidation depth, which is very similar to the homogeneous layer of the bulk oxidation zone. Little to no signs of grain boundary oxidation could be observed in the cases of Fe-3Al-1Si and Fe-1Si-0.8Cr where the cross section only shows a distinct 3-4 μm thick band of bulk oxides underneath the sample surface.

(FIGURE 3)

SEM analyses of the cross sections in figure B.4 revealed the presence of finely dispersed oxides inside the grains, that compose the bulk oxidation band (i.e. the grey shaded area in figures B.3 and B.4). Grain boundary oxides showed to be up to 250 nm thick and mostly continuously distributed along the grain boundaries. Individual oxide particles that align along the

grain boundaries could only be seen in the case of Fe-2Mn-0.8Cr. The microstructure near the sample surface of all alloys seems to be composed of smaller ferrite grains than in the interior near the oxidation front. This may be attributed to grain boundary pinning by the newly formed oxides in the early stages of the experiment [46]. As a consequence, recrystallisation during the heat treatment at 700 °C will be blocked as soon as oxides are present. This effect is dominant in close proximity to the surface and loses its influence towards the sample interior, since there has been more time for grain growth prior to grain boundary pinning by oxides. Occasionally, extremely fine oxide structures in sub-grain boundaries could be detected. These structures form as a tensile stress release mechanism that compensates the mechanical energy caused by the local volume increase due to oxide formation. Since the increase of molar volume is biggest in the case of silicon ($\Delta V_m = 10.63 \times 10^{-6}$ m^3 mol^{-1} for Si $\rightarrow$ SiO_2 [18, 47]), the visibility of sub-grain boundaries is dominant in silicon containing alloys.

(FIGURE 4)

Since oxygen diffuses from the surface towards the interior, the local oxygen activity decreases towards the sample interior and reaches a critical limit for oxide formation at the oxidation front. Close to the surface, the oxygen activity becomes higher which stabilises oxygen-rich precipitates such as spinels or mixed oxides of the alloy additions with iron (compare figure $B.5$). Such a behaviour could be confirmed by qualitative EDX analyses although this data is not shown because this technique detects a huge iron signal, owing to the relatively large measurement spot compared to the tiny oxide

particles. However, an increased alloy content near the oxidation front could be observed. This points to the presence of a lower iron content in the oxides (or even pure alloy element oxides) close to the oxidation front.

Calculations of the spatial phase distribution were carried out by using the pure substance thermodynamic dataset from FactSage [48]. As a consequence, the calculated phases possess the stoichiometric composition that is determined from the database. However, especially in the case of MnO, the cation sites in the crystal lattice can easily be occupied by either manganese or iron, which leads to the good miscibility of MnO and wüstite (FeO) [49]. This leads to a variation of the minimal oxygen activity, needed for formation of an oxide, depending on the local iron/manganese ratio. Assuming the thermodynamics of ideal mixing, one would expect for the oxide composition (1) an increased content of manganese towards the internal oxidation front (2) the formation of mixed iron-manganese oxides near (or at [18]) the surface with a manganese content, corresponding to the oxygen activity in the reaction gas.

(FIGURE 5)

Interstingly, the calculated oxidation depths are always larger than experimental observations. Whereas the biggest deviation of more than a factor of 2 has been measured in the absence of grain boundary oxidation, little to no deviation of the total oxidation depth could be observed for manganese containing alloys that show preferential grain boundary oxidation. Within this study, all alloys show a bulk oxidation behaviour that is significantly lower than expected from theoretical predictions. This strongly suggests inhibition

of the element transport inside the ferrite grains, which may again likely be caused by defect structures and element trapping [13, 39]. Whereas defects can decrease diffusion due to their trapping behaviour in a well-defined crystal lattice and also across grain boundaries in a wider sense, their influence almost vanishes along the diffuse grain boundary region at elevated temperatures [13, 15, 51] where the oxygen atoms "jump" from one defect site to the other without interactions with the ideal crystall lattice. While theoretical simulations only consider diffusion and local thermodynamic equilibria, oxygen isotope experiments help to shine light on the influence of substitution reactions in the fine-grained oxide precipitates [52, 53, 54]. This helps to unravel the pathways of fast oxygen transport in the alloy and leads towards the origin of the pronounced grain boundary oxidation in some alloys. Previous studies show that two hypothetical and extreme mechanisms determine the oxygen isotope distribution pattern - transport via diffusion (including fast diffusion pathways) and oxygen isotope substitution in the already formed oxide precipitates. A pure oxygen isotope substitution mechanism under the conditions shown in figure B.6 would lead to two separated oxide regions, where the upper layer near the sample surface just contains ^{18}O. This domain "pushes" the ^{16}O-isotopes further inwards during thermal treatment, which can then be found directly underneath the ^{18}O layer. Consequently, the presence of ^{16}O determines the total oxidation depth in the alloy. A pure diffusion mechanism without substitution implies that ^{18}O-isotopes move inwards and form oxides near the oxidation front. In this case, no changes of the ^{16}O-distribution would be observed - ^{16}O being firmly bonded at its original sites - and the total oxidation depth is then defined by the innermost

presence of ^{18}O-isotopes.

(FIGURE 6)

Clear signs of fast oxygen diffusion along the grain boundary domain could be seen in all manganese containing alloys (figure B.6, left column). The majority of ^{18}O passes the region of previously formed ^{16}O-oxides along the grain boundaries with little to no oxygen isotope substitution. This indicates that oxygen transport along grain boundaries has only little interaction with oxygen diffusion through the ferrite grains. Slight signs of grain boundary oxidation could be detected in Fe-3Al-0.8Cr. Consequently we conclude that the grain boundaries act as a channel of fast oxygen transport through the internal precipitate zone, leading to an increased amount of ^{18}O-oxides near the oxidation front. Similar to the pronounced diffusion mechanism along grain boundaries (with little to no oxygen isotope substitution), ^{18}O has to move through the ferrite grains and partially substitutes the oxygen isotopes (^{16}O by ^{18}O) in the bulk oxides. Consequently, the ^{18}O-region near the sample surface pushes the ^{16}O-oxide region further inwards, which becomes now sandwiched between two clearly visible ^{18}O-regions. This behaviour can nicely be seen in the case of Fe-3Al-1Si (figure B.6).

The fact, that predominant grain boundary oxidation could only be observed in the case of manganese alloys, suggests a significant influence of this element. In contrast to these findings, we found no signs of grain boundary oxidation in binary low alloyed iron-manganese (figure $B.2$) which has also been confirmed in previous studies [18, 55]. This leads to the consequence that not a single-element effect of manganese but the combination of manganese and additional alloy elements lead to the pronounced grain boundary

oxide formation. Manganese possess the unique possibility to quickly vary its valency states, which may allow for relatively fast ion transport in the oxide crystal. The fact, that surface energies may alter thermodynamic stability (and hence phase diagrams) [56] is likely not to be responsible for the fast oxygen diffusion along grain boundaries. The manganese free alloys in this study do not possess such a high redox-flexibility of the alloy element's valency states (or do not form mixed oxides at all) and hence show little to no oxidative attack along grain boundaries. Another possibility is to attribute the result to a convolute effect of enhanced element transport along grain boundaries and an overall lower oxygen diffusion due to interaction with defects in the ferrite lattice. Such an explanation, however, would imply that the oxygen-trap-interaction in the diffuse grain boundary domain is similar to interaction in the well-ordered crystal lattice, which seems very unlikely. It needs to be emphasised that the experimental approach presented here may not strictly reflect the behaviour underneath a dense wüstite layer for typical industrial conditions. In an industrial process, the oxygen activity at the metal-scale interface is defined by the oxygen transport properties through the outer scale layer as well as by wüstite decomposition kinetics [24]. These barriers may lead to a significant decrease of the local oxygen activity in the metal and alter the formation of oxides. However, the present study describes the internal oxidation behaviour of iron-based alloys at elevated temperatures in such a pure and simple way that results may even be used to extend theoretical knowledge by the synergies of ternary element additions.

5. Conclusions

Selective oxidation experiments at 700 °C in binary and ternary iron-based alloys, containing Al, Cr, Mn and Si have been performed. Cross sections of all ternary iron-manganese based samples revealed a fine network of up to 250 nm thick grain boundary oxides that separate individual grains and show severest oxidative attack (7-11 μm). The fact, that pronounced grain boundary oxidation is absent in binary Fe-2Mn, may partially be due to the formation of sparsely distributed oxides at the surface of the Fe-2Mn samples. However, this is more likely to be an effect of mixed oxide formation in ternary alloy compositions (Al, Cr or Si) with Mn.

Bulk oxidation behaviour (oxide formation inside the ferrite grains) became dominant in Fe-{1, 3}Al, Fe-2Mn as well as ternary manganese-free alloys, characterised by the presence of finely dispersed oxide particles that reach up to 4 μm into the material. An intermediate case of bulk oxidation with slight signs of grain boundary oxidation was observed in Fe-3Al-0.8Cr.

Remarkably, only minor discrepancies of $\leq$1 μm between simulations and experiments could be verified in alloys that show pronounced grain boundary oxidation. This behaviour is attributed to trapping reactions in the grain that effectively slow down bulk diffusion behaviour (predominantly oxygen diffusion). Hence, the diffuse crystal structure near grain boundaries at elevated temperatures favours fast oxygen transport along (but not across!) them, and does not exceed the limit of pure grain boundary diffusion data from literature.

"Enhanced grain boundary oxidation" - which is often found in the literature - would be misleading in the present case as one might expect a diffusion

mechanism that is faster than theoretical expectations. Findings in Fe-0.8Cr, Fe-1Si and ternary iron-manganese alloys rather suggest that diffusion along grain boundaries does not change much by crystal defects. However, pure bulk oxidation was indeed slowed down in all other alloys.

Oxygen isotope exchange experiments prove the fast diffusion pathways along grain boundaries and the small interaction between grain boundary oxides and oxide particles inside the grains. Here, the ^{18}O-isotope signal along grain boundaries in ternary iron-manganese based alloys was predominant, compared to the ^{16}O signal. Oxygen isotope exchange becomes significant in the absence of grain boundary oxides, leading to the formation of an internal ^{16}O region. An intermediate situation between fast oxygen transport and oxygen isotope substitution could be observed in Fe-3Al-1Si, where the ^{16}O domain is sandwiched between two ^{18}O domains.

Since Al, Cr and Si form stiochiometric oxides due to their low flexibility in their valency state (compared to Mn), fast oxygen transport along grain boundaries may likely be caused by the formation of mixed oxides with Mn (ternary alloys) and/or the atomic structure in the metal near the grain-oxide interface (Fe-0.8Cr, Fe-1Si).

6. Acknowledgements

The authors thank M. DeBardi, K. Piplits and Prof. H. Hutter (all Vienna University of Technology) for their assistance with the ToF-SIMS measurements. Helpful support with the thermal insulation of the pressurised gas mixing chamber by S. Evers and D. Vogel (both Max-Planck-Institut für Eisenforschung GmbH) is greatfully acknowledged. M. Auinger is thankful

to D. Paesold (voestalpine Stahl GmbH) and Prof. J. Fleig (Vienna University of Technology) for scientific discussions. Financial support by the voestalpine Stahl GmbH (Austria) and the Christian Doppler Forschungsgesellschaft (Austria) for the Christian Doppler Laboratory, led by M. Rohwerder (Max-Planck-Institut für Eisenfoschung GmbH), is gratefully acknowledged.

Appendix A. Binary Phase Diagrams

(FIGURE 7)

Appendix B. Ternary Phase Diagrams

(FIGURE 8)

References

[1] N. Birks, G.H. Meier, F.S. Pettit, Introduction to High Temperature Oxidation of Metals, second ed. Cambridge: Cambridge University Press, 2006.

[2] D.J. Young, High Temperature Oxidation and Corrosion of Metals, in: Burstein T (Eds.). Elsevier Corrosion Series. Oxford: Elsevier, 2008.

[3] P.J. Meschter, E.J. Opila, N.J. Jacobson, Water Vapor-Mediated Volatilization of High-Temperature Materials, Annu. Rev. Mater. Res. 43 (2013) 559-588.

[4] E. Essuman, G.H. Meier, J. Żurek, M. Hänsel, L. Singheiser, W.J. Quadakkers, Enhanced internal oxidation as trigger for breakaway oxidation of Fe-Cr alloys in gases containing water vapor, Scipta Mater. 57 (2007) 845-848.

[5] Grabke HJ, Schütze M, Oxidation of Intermetallics, second edn., Weinheim: Wiley VCH, 2008.

[6] M. Sánchez Pastén, M. Spiegel, High temperature corrosion of metallic materials in simulated waste incineration environments at 300 - 600 °C, Mater. Corros. 57 (2006) 192-195.

[7] A.H. Heuer, D.B. Hovis, J.L. Smialek, B. Gleeson, Alumina Scale Formation: A New Perspective, J. Am. Ceram. Soc. 94 (2011) 146-153.

[8] E. Essuman, G.H. Meier, J. Żurek, M. Hänsel, W.J. Quadakkers, The Effect of Water Vapor on Selective Oxidation of Fe-Cr Alloys, Oxid. Met. 69 (2008) 143-162.

[9] O. Grässel, L. Krüger, G. Frommeyer, L.W. Meyer, High strength Fe-Mn-(Al,Si) TRIP/TWIP steels development - properties - application, Int. J. Plasticity 16 (2000) 1391-1409.

[10] P. Hou, Segregation Phenomena at Thermally Grown Al_2O_3/Alloy Interfaces, Annu. Rev. Mater. Res. 38 (2008) 275-298.

[11] M. Hänsel, C.A. Boddington, D.J. Young, Internal oxidation and carburisation of heat-resistant alloys, Corros. Sci. 45 (2003) 967-981.

[12] L. Liu, Z.G. Yang, C. Zhang, M. Ueda, K. Kawamura, T. Maruyama, Effect of water vapour on the oxidation of Fe-13Cr-5Ni martensitic alloy at 973 K, Corros. Sci. 60 (2012) 90-97.

[13] B. Pieraggi, R.A. Rapp, J.P. Hirth, Role of Interface Structure and Interfacial Defects in Oxide Scale Growth, Oxid. Met. 44 (1995) 63-79.

[14] I. Kaur, Y. Mishin, W. Gust, Fundamentals of Grain and Interphase Boundary Diffusion, third edn. Weinheim: John Wiley & Sons, 1995.

[15] P.L. Williams, Y. Mishin, Thermodynamics of grain boundary premelting in alloys. II. Atomistic simulation, Acta Mater. 57 (2009) 3786-3794.

[16] A. Atkinson, A Theoretical Analysis of the Oxidation of Fe-Si Alloys, Corros. Sci. 22 (1982) 87-102.

[17] B.A. Pint, I. Wright, The Oxidation Behavior of Fe-Al Alloys, Mat. Sci. Forum. 461-464 (2004) 799-806.

[18] M. Auinger, E.M. Müller-Lorentz, M. Rohwerder, Modelling and experiment of selective oxidation and nitridation of binary model alloys at 700 °C - The systems Fe, 1 wt.%{Al, Cr, Mn, Si}, Corros. Sci. 90 (2015) 503-510.

[19] D.J. Young, J. Zurek, L. Singheiser, W.J. Quadakkers, Temperature dependence of oxide scale formation on high-Cr ferritic steels in Ar-H_2-H_2O, Corros. Sci. 53 (2011) 2131-2141.

[20] H.J.T. Ellingham, Reducibility of Oxides and Sulphides in Metallurgical Processes, J. Soc. Chem. Ind.-L 5 (1944) 125-133.

[21] M. Auinger, A. Vogel, V.G. Praig, H. Danninger, M. Rohwerder, Thermogravimetry and insitu mass spectrometry at high temperatures compared to thermochemical modelling - The weight loss during selective decarburisation at 800 °C, Corros. Sci. 78 (2014) 188-192.

[22] A. Holt, P. Kofstad, Electrical conductivity and defect structure of Cr_2O_3 I. High temperatures (<≈1000°C), Solid State Ionics 69 (1994) 127-136.

[23] F. Millot, Y. Niu, Diffusion of ^{18}O in Fe_3O_4: An Experimental Approach to Study the behavior of Minority Defects in Oxides, J. Phys. Chem. Solids. 58 (1997) 63-72.

[24] M.H. Davies, M.T. Simnad, C.E. Birchenall, On the Mechanism and Kinetics of the Scaling of Iron, T. Metall. Soc. AIME 10 (1951) 889-896.

[25] T.J. Nijdam, L.P.H. Jeurgens, W.G. Sloof, Modelling the thermal oxidation of ternary alloys-compositional changes in the alloy and the development of oxide phases, Acta Mater. 51 (2003) 5295-5307.

[26] M. Auinger, P. Ebbinghaus, A. Blümich, A. Erbe, Effect of surface roughness on optical heating of metals, J. Europ. Opt. Soc. Rap. Public. 9 (2014) 14004.

[27] M. Auinger, D. Vogel, A. Vogel, M. Spiegel, M. Rohwerder, A novel laboratory set-up for investigating surface and interface reactions during short term annealing cycles at high temperatures, Rev. Sci. Instr. 84 (2013) 085108.

[28] B.L. Bramfitt, A.O. Benscoter, Metallographer's Guide - Practice and Procedures for Irons and Steels, first edn., Materials Park Ohio: ASM International, 2002.

[29] M. Auinger, R. Naraparaju, H.J. Christ, M. Rohwerder, Modelling High Temperature Oxidation in Iron-Chromium Systems: Combined Kinetic and Thermodynamic Calculation of the Long-Term Behaviour and Experimental Verification, Oxid. Met. 76 (2011) 247-258.

[30] W.M. Pragnell, H.E. Evans, A finite-difference model to predict 2D depletion profiles arising from high temperature oxidation of alloys, Modelling Simul. Mater. Sci. Eng. 14 (2006) 733-740.

[31] H. Mehrer, Landolt Börnstein - Numerical Data and Functional Relationships in Science and Technology: Group III, vol. 26, Berlin: Springer, 1990.

[32] J.H. Swisher, E.T. Turkdogan, Solubility, Permeability, and Diffusivity of Oxygen in Solid Iron, T. Metall. Soc. AIME 239 (1967) 426-431.

[33] C. Wagner, Theoretical Analysis of the Diffusion Processes Determining the Oxidation Rate of Alloys, J. Electrochem. Soc. 99 (1952) 369-380.

[34] U. Krupp, H.J. Christ, Selective Oxidation and Internal Nitridation during High-Temperature Exposure of Single-Crystalline Nickel-Base Superalloys, Metall. Mater. Trans. A 31 (2000) 47-56.

[35] D. Huin, P. Flauder, J.B. Leblond, Numerical Simulation of Internal Oxidation of Steels during Annealing treatments, Oxid. Met. 64 (2005) 131-167.

[36] S. Petersen, K. Hack, The thermochemistry library ChemApp and its applications, Int. J. Mat. Res. 98 (2007) 935-945.

[37] M. Auinger, A. Vogel, D. Vogel, M. Rohwerder, Early stages of oxidation observed by in situ thermogravimetry in low pressure atmospheres, Corros. Sci. 86 (2014) 183-188.

[38] H. Kokawa, M. Shimada, Y.S. Sato, Grain-Boundary Structure and Precipitation in Sensitized Austenitic Stainless Steel, JOM 52 (2000) 34-37.

[39] M. Auinger, Hydrogen Transport in non-ideal Crystalline Materials, Chem Phys Chem 15 (2014) 2893-2902.

[40] H.J. Grabke, Surface and Grain Boundary Segregation on and in Iron and Steels, ISIJ Int. 29 (1989) 529-538.

[41] P. Lejček, Grain Boundary Segregation in Metals, in: Hull R, Parisi J, Jagadish C, Wang Z, Osgood RM, Warlimont H (Eds.). Springer Series in Materials Science. Heidelberg: Springer-Verlag, 2010.

[42] D.J. Young, M.L. Burg, P.R. Munroe, Internal Precipitation of Al_2O_3 and Cr_2O_3 in Austenitic Alloys, Mat. Sci. Forum 461-464 (2004) 21-28.

[43] W. Zhao, Z. Li, B. Gleeson, A New Kinetics-Based Approach to Quantifying the Extent of Metastable → Stable Phase Transformation in Thermally-Grown Al_2O_3 Scales, Oxid. Met. 79 (2013) 361-381.

[44] J. Töpfer, S. Aggarwal, R. Dieckmann, Point defects and cation tracer diffusion in $(Cr_xFe_{1-x})_{3-\delta}O_4$ spinels, Solid State Ionics 81 (1995) 251-266.

[45] E.J. Opila, Oxidation and Volatilization of Silica Formers in Water Vapor, J. Am. Ceram. Soc. 86 (2003) 1238-1248.

[46] Ö.N. Dogan, G.M. Michal, H.W. Kwon, Pinning of Austenite Grain Boundaries by AlN Precipitates and Abnormal Grain Growth, Metall. Mater. Trans. A 23 (1992) 2121-2129.

[47] D.R. Lide, CRC Handbook of Chemistry and Physics, CRC Press, Boca Raton, FL; 2010 Internet Version (http://www.hbcpnetbase.com).

[48] C.W. Bale, P. Chartrand, S.A. Degterov, G. Eriksson, K. Hack, R. Ben Mahfoud, J. Melanon, A.D. Pelton, S. Petersen, FactSage Thermochemical Software and Databases, Calphad 26 (2002) 189-228.

[49] W.K. Chen, N.L. Peterson, Effect of the Deviation from Stoichiometry on Cation Self-Diffusion and Isotope Effect in Wüstite, $Fe_{1-x}O$, J. Phys. Chem. Solids 36 (1975) 1097-1103.

[50] Y. Takada, S. Shimada, J. Lee, M. Kurosaki, T. Tanaka, The Effect of Si and Mn Content on Dynamic Wetting of Steel with Liquid Zn, ISIJ Int. 49 (2009) 100-104.

[51] A. Atkinson, Grain-boundary Diffusion: An Historical Perspective, J. Chem. Soc. Faraday Trans. 86 (1990) 1307-1310.

[52] B.A. Pint, J.R. Martin, L.W. Hobbs, ^{18}O/SIMS Characterization of the Growth Mechanism of Doped and Undoped α-Al_2O_3, Oxid. Met. 39 (1993) 167-195.

[53] K. Bongartz, W.J. Quadakkers, J.P. Pfeifer, J.S. Becker, Mathematical modelling of oxide growth mechanisms measured by ^{18}O tracer experiments, Surf. Sci. 292 (1993) 196-208.

[54] A.H. Heuer, T. Nakagawa, M.Z. Azar, B.D. Hovis, J.L. Smialek, B. Gleeson, N.D.M. Hine, H. Guhl, H.S. Lee, P. Tangney, W.M.C. Foulkes, W.M. Finnis, On the growth of Al_2O_3 scales, Acta Mater. 61 (2013) 6670-6683.

[55] P. Jackson, G. Wallwork, High Temperature Oxidation of Iron-Manganese-Aluminum Based Alloys, Oxid. Met. 21 (1984) 135-170.

[56] J. Olives, Surface thermodynamics, surface stress, equations at surfaces and triple lines for deformable bodies, J. Phys. Condens. Matter 22 (2010) 085005.

Table B.1: Alloy compositions, measured by atomic absorption spectroscopy (AAS, values with * were not measured).

Nominal Composition	Al (wt-%)	Cr (wt-%)	Mn (wt-%)	Si (wt-%)	Fe
Fe-1Al	1.10	<0.002	0.023	<0.005	bal.
Fe-3Al	2.70	*	*	*	bal.
Fe-0.8Cr	<0.003	0.80	<0.002	<0.005	bal.
Fe-2Mn	*	*	2.14	*	bal.
Fe-1Si	*	*	*	0.98	bal.
Fe-2Mn-1Al	1.00	<0.002	2.22	<0.005	bal.
Fe-2Mn-0.8Cr	*	0.79	2.17	*	bal.
Fe-2Mn-1Si	*	*	1.99	0.91	bal.
Fe-3Al-0.8Cr	2.84	0.82	*	*	bal.
Fe-3Al-1Si	2.82	<0.002	0.004	0.99	bal.
Fe-1Si-0.8Cr	0.012	0.92	*	1.02	bal.

Table B.2: Diffusion values and solubilities, used for the simulations.

Element Transport					
Element	bulk diffusion		grain boundary diffusion		Ref.
	D_0 / m^2 s^{-1}	Q / kJ mol^{-1}	$s\delta D_0$ / m^3 s^{-1}	Q / kJ mol^{-1}	
Iron (Fe)	1.21×10^{-2}	281.6	6.79×10^{-13}	174.0	[31]
Oxygen (O)	3.72×10^{-6}	42.40	3.72×10^{-12}	42.40[a]	[31, 32]
Aluminium (Al)	1.8×10^{-4}	228.2	1.8×10^{-10}	228.2[a]	[31]
Chromium (Cr)	8.52×10^{-4}	250.8	6.02×10^{-11}	217.7	[31]
Manganese (Mn)	7.60×10^{-5}	224.6	1.10×10^{-12}	192.9[b]	[31]
Silicon (Si)	1.7×10^{-4}	229.1	1.7×10^{-10}	229.1[a]	[31]
Solubility					
Element	c_0 / mol m^{-3}	Q_L / kJ mol^{-1}	$c_{(700°C)}$ / mol m^{-3}		Ref.
Oxygen (O)	3.034×10^4	95.72	$0.2209 \times p_{(H_2O)}/p_{(H_2)}$		[32]

[a] values set to 100 times the bulk diffusion coefficient due to missing data ($\delta = 10$ nm).

[b] values for polycrystalline Fe, 25wt-%Ni, 20wt-% Cr due to missing data in ferrite.

Table B.3: Experimental (d_{exp}) and calculated (d_{sim}) corrosion depth and presence of grain boundary oxides (GB-oxides) in binary and ternary iron-based alloys after heat treatment at 700°C for 60min in Ar / 2.5vol-%H_2 / 0.94vol-%H_2O.

Alloy	GB-oxides	d_{exp} (μm)		d_{sim} (μm)		d_{exp}/d_{sim}	
		bulk	GB	bulk	GB	bulk	GB
Fe-1Al	No	1.5	*	7.3	8.8	0.210	*
Fe-3Al	No	1.2	*	4.0	5.3	0.305	*
Fe-0.8Cr	Yes	1.1	2.8	10.8	13.9	0.106	0.201
Fe-2Mn	No	1.7	*	9.8	11.7	0.177	*
Fe-1Si	Yes	1.5	3.1	5.5	7.3	0.273	0.419
Fe-2Mn-1Al	Yes	2.4	8.2	6.3	8.9	0.386	0.920
Fe-2Mn-0.8Cr	Yes	1.5	7.4	7.6	9.2	0.196	0.800
Fe-2Mn-1Si	Yes	1.5	10.2	5.3	10.2	0.281	0.993
Fe-3Al-0.8Cr	slightly	3.1	4.5	4.6	8.5	0.674	0.528
Fe-3Al-1Si	No	2.5	*	4.3	8.5	0.573	*
Fe-1Si-0.8Cr	No	2.5	*	5.8	9.9	0.433	*

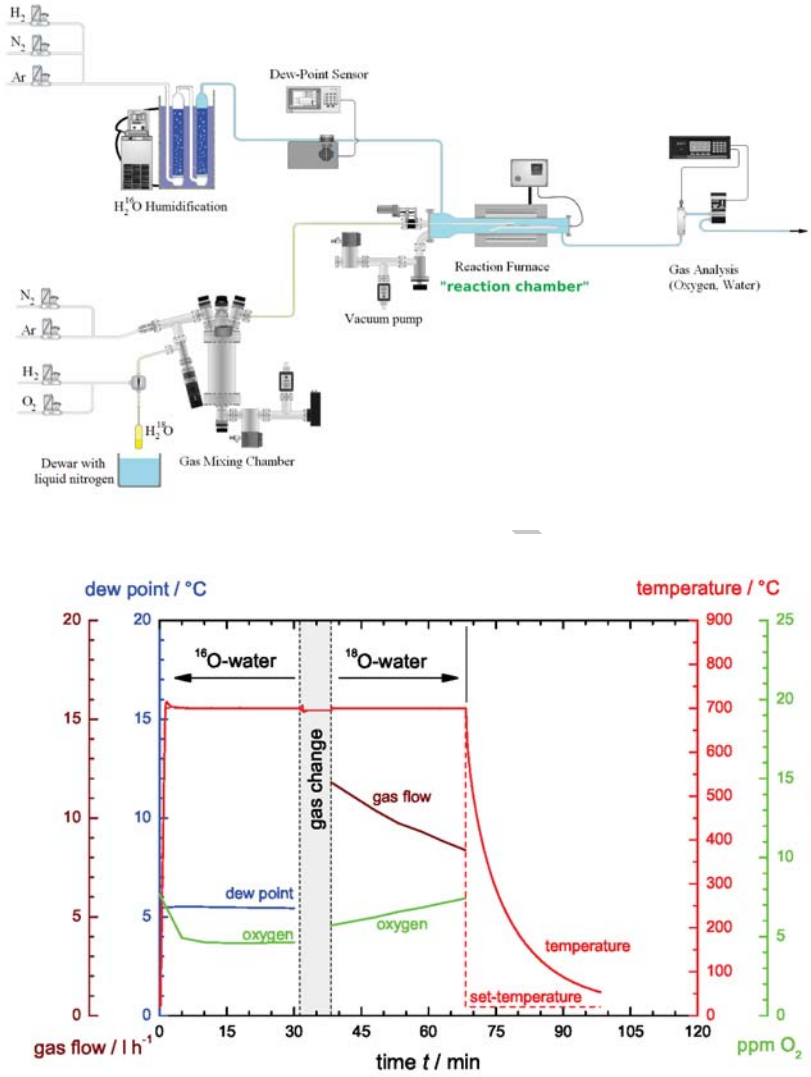

Figure B.1: Experimental set-up for high temperature reactions with fast gas changes (top) and parameters for high temperature oxidation of ternary iron alloys in Ar / 2.5vol-% H_2 with oxygen marked water vapour (0.94vol-% H_2O, DP +6 °C, $p_{(O_2)} = 2 \times 10^{-22}$ bar, bottom).

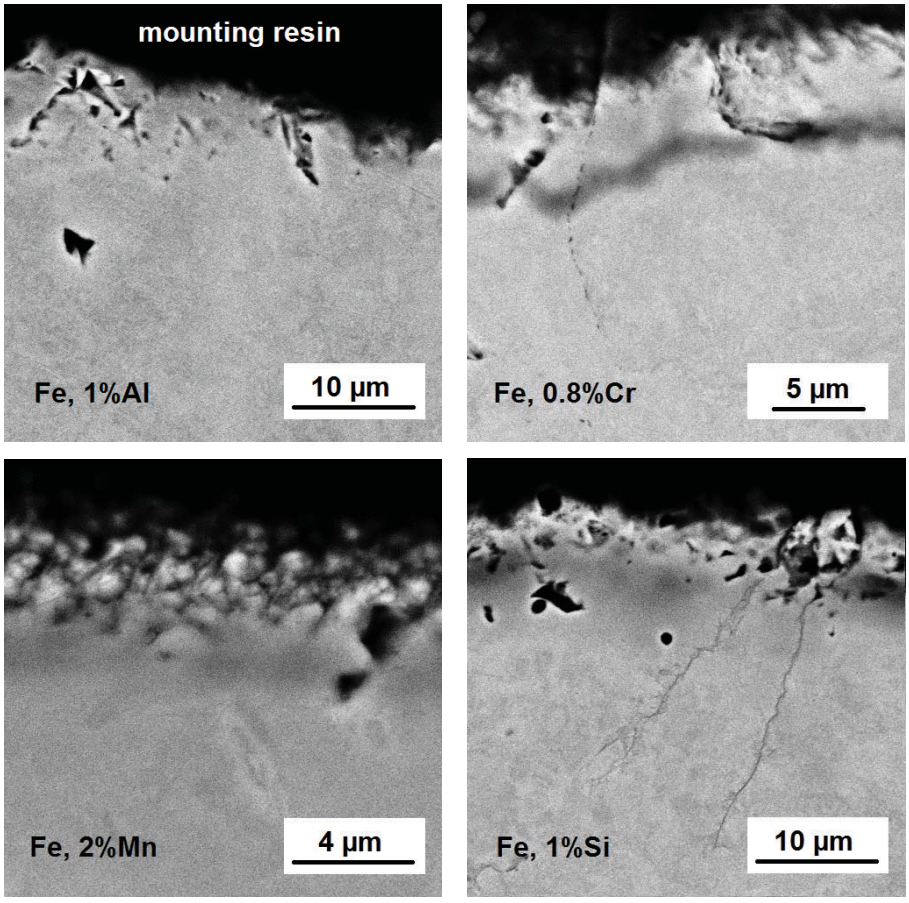

Figure B.2: SEM images of binary iron alloys, oxidised at 700°C in Ar / 2.5vol-% H_2 / H_2O (DP+6°C, 9400 ppm, $p_{(O_2)} = 2 \cdot 10^{-22}$bar) for a total time of 60 min. The cross sections were prepared with a 10° tilt angle, to enlarge the vertical view of the oxidised zone by a factor of 5.67.

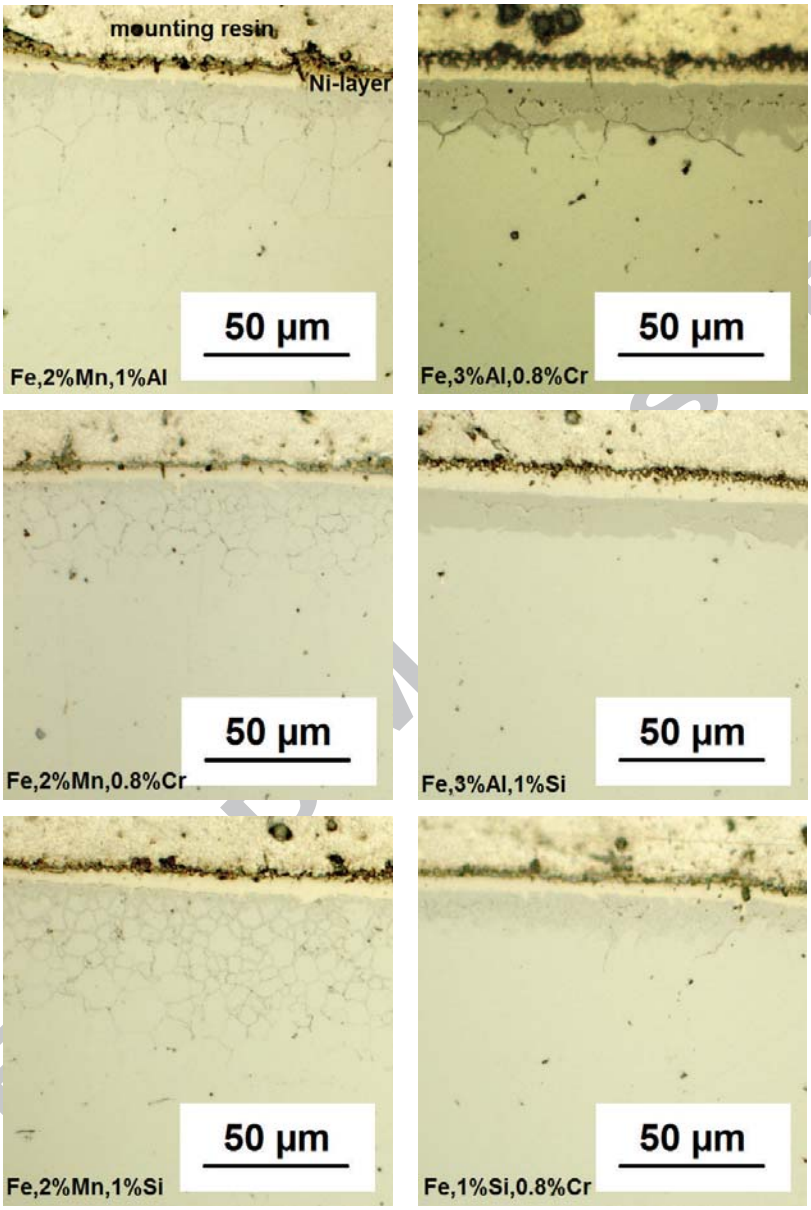

Figure B.3: Light optical microscopy images of ternary iron alloys, oxidised at 700 ° in Ar / 2.5vol-% H_2 / 0.94vol-% H_2O (DP +6 °C, $p_{(O_2)} = 2 \times 10^{-22}$ bar) for a total time of 60 min. The cross sections were prepared with a 10° tilt angle, to enlarge the vertical view of the oxidized zone by a factor of 5.67.

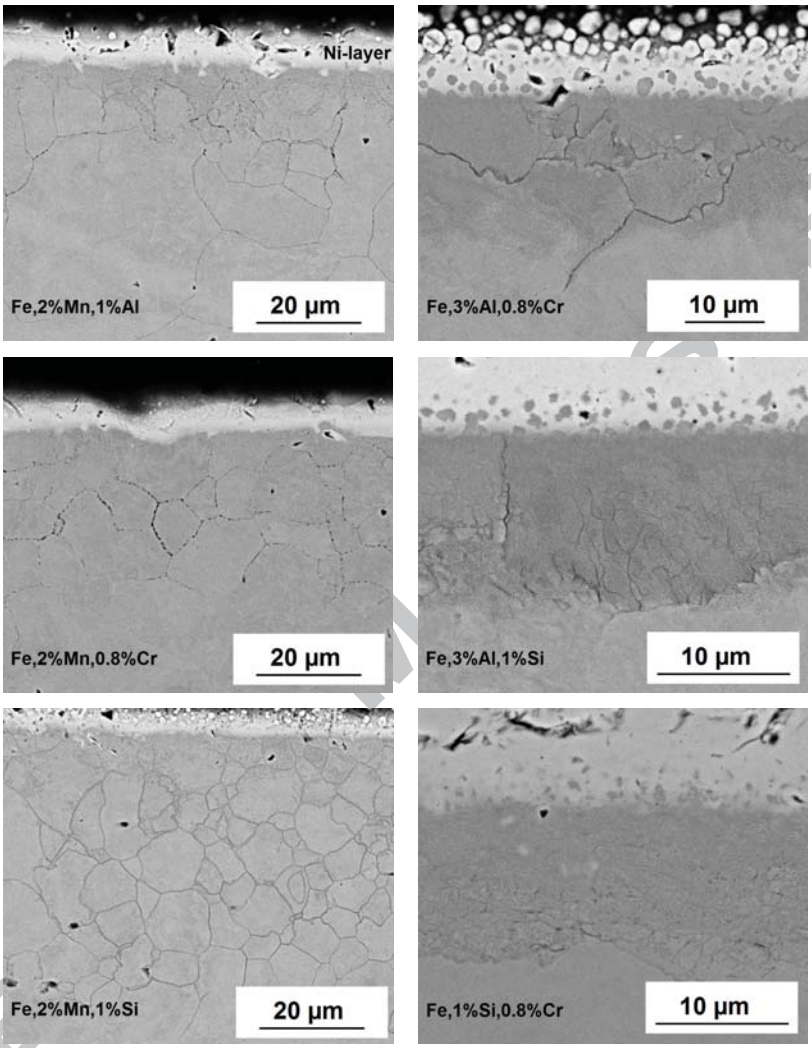

Figure B.4: SEM images of ternary iron alloys, oxidised at 700°C in Ar / 2.5vol-% H_2 / 0.94vol-% H_2O (DP +6 °C, $p_{(O_2)} = 2 \times 10^{-22}$ bar) for a total time of 60 min. The cross sections were prepared with a 10° tilt angle, to enlarge the vertical view of the oxidized zone by a factor of 5.67.

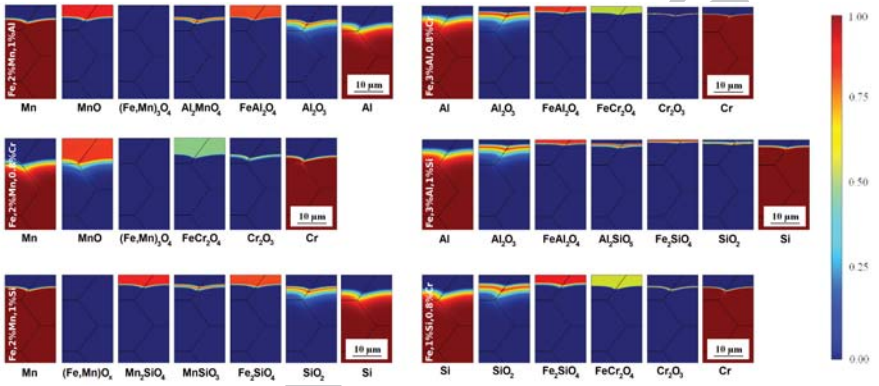

Figure B.5: Calculated spatial distribution of thermodynamically stable alloy element phases in ternary iron alloys, oxidised at 700 °C for 60 min in Ar / 2.5vol-% H_2 / 0.94vol-% H_2O (DP +6 °C, $p_{(O_2)} = 2 \times 10^{-22}$ bar). The values are normalised to the maximum amount of each phase ($c_{max} = 1$).

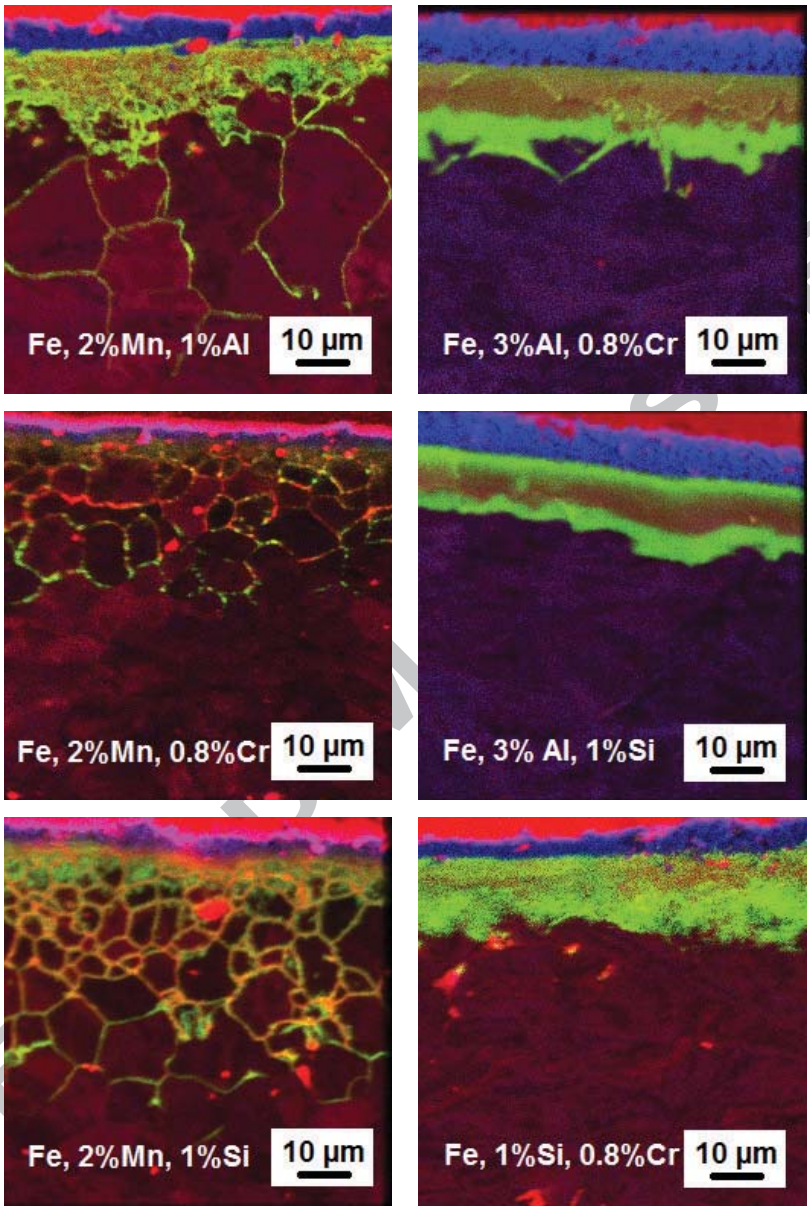

Figure B.6: ToF-SIMS measurements of oxygen isotope distribution in ternary iron alloys, oxidised at 700 °C for 60 min in Ar / 2.5vol-% H_2 / 0.94vol-% H_2O (DP +6 °C, $p_{(O_2)} = 2 \times 10^{-22}$ bar). After 30 min, the gas mixture for the heat treatment was switched from $H_2^{16}O$ to $H_2^{18}O$. The distributions are displayed for ^{18}O (green), ^{16}O (red) and Ni (blue). The top red part in the pictures is due to the embedding material. Cross sections were prepared with a 10° tilt angle, to enlarge the vertical view of the oxidized zone by a factor of 5.67.

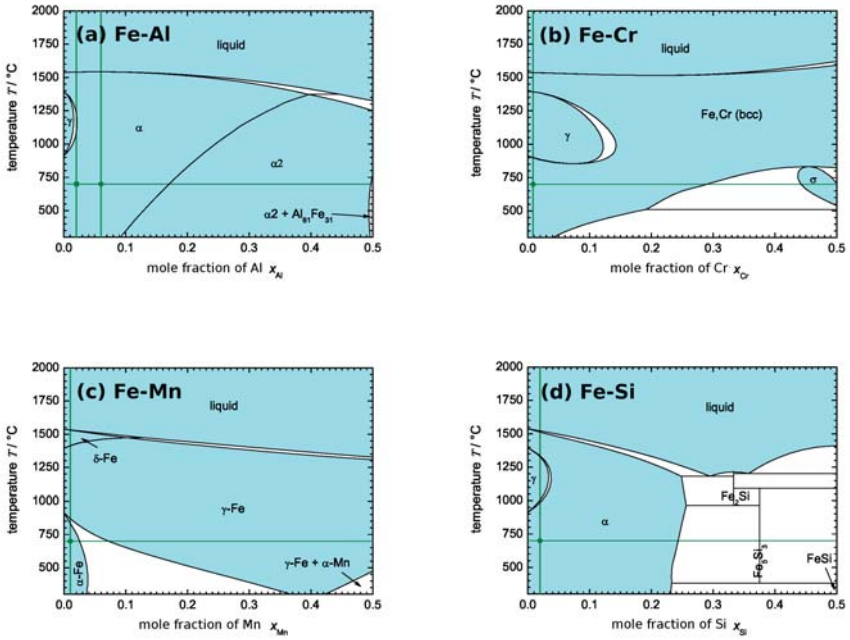

Figure B.7: Binary phase diagrams of iron-based alloys Fe-Al (a), Fe-Cr (b), Fe-Mn (c) and Fe-Si (d), calculated with FactSage [48]. The single phase regions are shown in blue. Compositions of the model alloys , Fe-0.8wt%Cr, Fe-1wt%{Al, Si}, Fe-2wt%Mn and Fe-3wt%Al are marked with green dots.

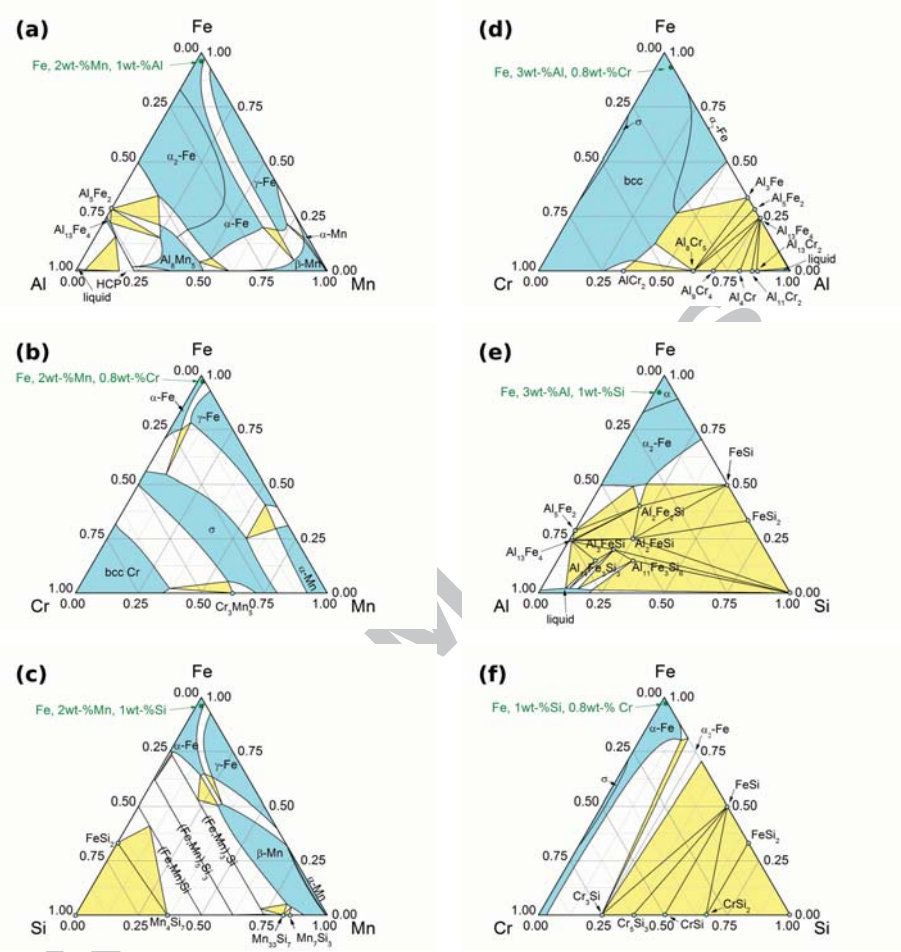

Figure B.8: Ternary phase diagrams of iron-based alloys Fe-Mn-Al (a), Fe-Mn-Cr (b), Fe-Mn-Si (c), Fe-Al-Cr (d), Fe-Al-Si (e) and Fe-Cr-Si (f) at 700 °C, calculated with FactSage [48]. Phase regions are marked by following the suggestion of The American Society of Metallurgists (single phase region - blue, three phase region - yellow). Compositions of iron based model alloys, used for this study, are marked with green dots.

Highlights for Review

- Selective oxidation at 700°C in iron-based model alloys
- Variation of the oxygen isotopes (^{16}O/ ^{18}O) to determine fast diffusion pathways
- Mn containing ternary alloys show severe grain boundary oxidation
- Grain boundary oxidation similar to theoretical results but bulk oxidation smaller
- Substitution between bound (oxide) and mobile oxygen observed in Mn-free alloys